![TESCAN logo]
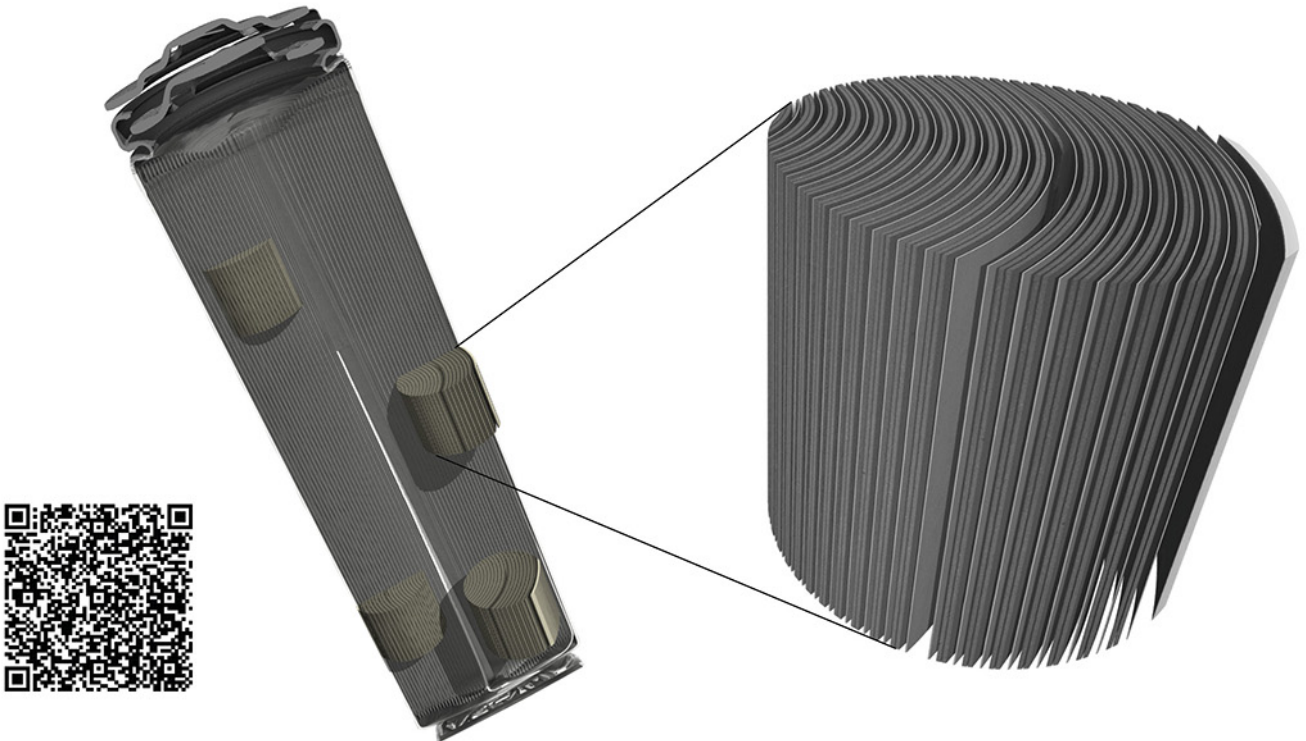
TESCAN micro-CT solutions
for energy storage materials research

TESCAN UniTOM XL

- ✓ Multi-scale non-destructive 3D imaging optimized to maximize throughput and contrast

- ✓ Fast scanning and high sample throughput with temporal resolutions below 10 seconds

- ✓ Wide array of samples types

- ✓ Enables dynamic tomography and *in-situ* experiments

- ✓ Dynamic screening for synchrotron beamtime

- ✓ Modular and open system with unmatched flexibility for research

TESCAN UniTOM XL

Click and find out more

Auto-Switching Self-Powered System for Efficient Broad-Band Wind Energy Harvesting Based on Dual-Rotation Shaft Triboelectric Nanogenerator

Shun Yong, Jiyu Wang,* Lijun Yang, Hanqing Wang, Hao Luo, Ruijin Liao, and Zhong Lin Wang*

A triboelectric nanogenerator (TENG) based self-powered system for wind energy harvesting introduces a desirable solution to alleviate the expanding energy supply concerns in the development of the internet of things. In this work, an auto-switching self-powered system based on a dual-rotation shaft TENG (D-TENG) is reported to effectively harvest wind energy over a broad-band wind speed (2.2–16 m s^{-1}). The D-TENG is designed in a concentric dual-rotation shaft structure, in which two independent TENGs with different shapes, sizes, and arm lengths of wind cups are rationally coupled. The integration of the two TENGs with varied structural parameters achieves mutual compensation of their own merits, enabling the whole system to have preferable aerodynamics and high energy conversion efficiency over a broad range of wind speeds. Moreover, an electromagnetic generator (EMG) with the same energy collection module is also fabricated for a comparison with TENG in the start-up properties and average output power. Furthermore, a packaged self-powered system is demonstrated for simulated wind energy harvesting, while the charging characteristics are also discovered. The proposed TENG renders a more efficient technique for energy harvesting and greatly expands its potential in the large-scale wind energy harvesting that can be attributed to the multi-stage strategy.

1. Introduction

The swift development of the Internet of Things has aroused urgent demands for powering trillions number of widely distributed sensors that can monitor every aspect of human lives reliably and autonomously.[1–5] The deficiencies of conventional battery-based sensors such as limited lifetime, risk of environmental pollution, and low device maintainability[6,7] have been gradually exposed to be insufficient to settle down the explosive increase of these decentralized sensors. Thus, self-powered technology that harvests environmental energy as sustainable power supply has become an attractive and sustainable solution to the restraints of conventional power supply.[8–11] Among all types of ambient energy, wind energy is regarded as the most ubiquitous and sustainable energy source in our daily life with huge quantities.[12–15] Traditionally, the wind energy generally refers to medium and strong winds with wind speeds over 4.0 m s^{-1}, which is an efficient working range for most of wind harvesting technologies.[16–19] However, the global average wind speed near the surface with an observation altitude of 10 m in height is reported to be 3.28 m s^{-1},[10,18] which implies the inadequate utilization of the most prevalent wind energy resources in low wind speed by current technology. In decades, wind power generations with electromagnetic generators (EMGs) have been widely used in the wind farm,[20,21] but still difficult to apply in distributed miniature power supply for their bulky and heavy inherent

S. Yong, Dr. J. Wang, Prof. L. Yang, H. Wang, H. Luo, Prof. R. Liao
State Key Laboratory of Power Transmission Equipment and
System Security and New Technology
Chongqing University
Shapingba, Chongqing 400044, P. R. China
E-mail: jiyuwang@cqu.edu.cn
Dr. J. Wang
Tsinghua-Berkeley Shenzhen Institute
Tsinghua Shenzhen International Graduate School
Tsinghua University
Shenzhen, Guangdong 518055, P. R. China

Prof. Z. L. Wang
Beijing Institute of Nanoenergy and Nanosystems
Chinese Academy of Sciences
Beijing 100083, P. R. China
E-mail: zhong.wang@mse.gatech.edu
Prof. Z. L. Wang
CUSPEA Institute of Technology
Wenzhou, Zhejiang 325024, P. R. China
Prof. Z. L. Wang
School of Material Science and Engineering
Georgia Institute of Technology
Atlanta, GA 30332, USA

iron-magnetic structure.[22,23] Different from EMGs, the triboelectric nanogenerators (TENGs), as driven by the Maxwell's displacement current, can effectively convert broadband wind energy, especially the low-speed band, into electricity based on the coupling of triboelectrification and electrostatic induction.[24–27] With the flexible structure and diverse materials, the TENGs exhibit unique merits of high voltage, high efficiency, lightweight, and low fabrication cost for harvesting a variety of sources such as vibrations, water waves, and bioenergy, etc.[28–33] These features render the TENG to be a feasible technology to effectively harvest wind energy in a wide wind speed.

Previously, most TENG-based wind energy harvester prototypes have been designed into two main types, the trembling type and the rotating type.[34–37] The trembling type with the basic structure of internal film accompanied by top and bottom electrodes has been proposed to first convert wind energy into vibration energy by vibrating the internal film, then produce the electricity through the contact-separation movements during vibrations. However, the output value from the trembling type is hard to maintain stability due to the random signals produced by the irregular trembling movements, which is difficult to be integrated into a self-powered system for widespread applications. The rotating type on the contrary is able to collect and produce more stably, but it was found that the force driven by low wind speed cannot provide continuous kinetic energy for a complete friction cycle of TENG. In this case, it is challengeable for TENGs to operate under the circumstance of low wind speed. Previous research has therefore focused on enlarging the size of sensors or assembling turbo charger to enhance the torque under low wind speed at the cost of compact size. J. Wang[38] has modified the friction type by introducing a soft friction model that further reduces the kinetic energy required for one cycle of the TENG cycle, the adverse of friction however is hardly eliminated. In this regard, a comprehensive design strategy to obtain both high driven performance and output performance should be formulated.

It is generally accepted that if a TENG-based wind energy harvester could be made to satisfy breeze aerodynamics, it would necessarily be at the expense of other features, such as small size, light rotational hindrance of the rotor, or small frictional area. However, even with this compromised design, this breeze-driven device might not be efficient for all the broadband wind speeds. In fact, the TENG-based wind energy harvester normally designed with fixed kinetic energy collector is corresponding to a fixed energy capture internal, and therefore cannot be adapted to efficiently work in other intervals. Therefore, to maintain the high conversion efficiency at all wind speeds, the structural parameters of the energy capture device need to be adjusted in real time. Inspired by the gear shifting systems of automobiles, a multi-stage auto-switching energy harvesting device was proposed to achieve efficient power output at different wind speeds by assembling energy capturing modules with different structural parameters into a single unit. In this way, the different modules in the multi-stage structure are capable of harvesting the wind energy and converting them at the most efficiency within their own wind speed range, enabling the self-powered system to operate with an optimal output performance at a broader wind speed range.
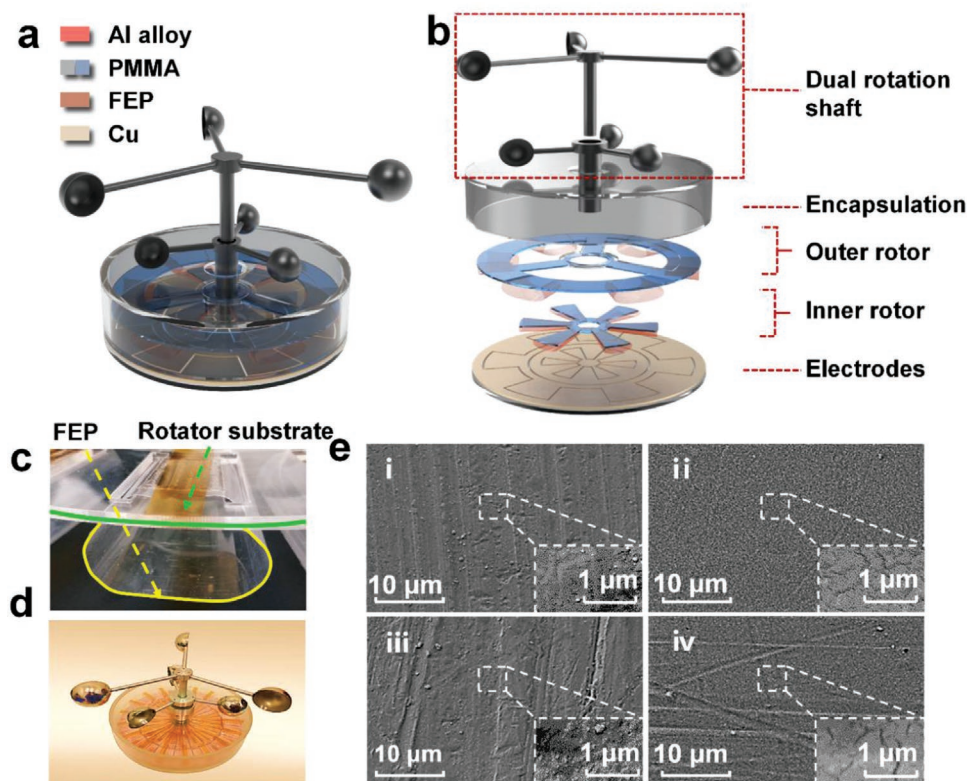
In this paper, an auto-switching self-powered system for efficient broad-band wind energy harvesting based on dual-rotation shaft TENG (D-TENG) is proposed. The D-TENG is designed in a concentric dual-rotation shaft structure, in which two independent TENGs with different shapes, sizes, and arm lengths of wind cups are integrated for realizing the multi-stage energy harvesting function. By integrating the TENGs together, this complementary aerodynamics and output performance enables the D-TENG to harvest wind energy and deliver satisfactory output in a broad range of wind speed. To further increase the aerodynamics and output performance of D-TENG, the devices with varied arm lengths, radiuses and pairs were experimentally compared. With the parameters optimization, we proposed an idea in search of optimal parameter combination for the multi-stage device with more integrated TENGs, which can be regarded as a design concept for fabricating this concentric planar-structured TENG with more rotary shafts. On the basis of this new design, the system can effectively collect wind energy with wind speeds ranging from 2.2 to 16 m s^{-1}, in which the start wind speed is only 2.2 m s^{-1}, and the switching wind speed is ≈5–6 m s^{-1}. For the electric performance, a maximum open-circuit voltage (V_{oc}) of 306 V and short-circuit current (I_{sc}) of 32 µA have been achieved, corresponding to a power output of 5.2 mW, which is capable of driving the commercial sensors and Wi-Fi module. Furthermore, the charge and discharge characteristics for the capacitive load were discovered, and practical applications were also demonstrated to show the feasibility of intermittent power supply for distributed sensors. This proposed concentric device with flexible structure can be easily upgraded to form a multi-stage nanogenerator unit in the same volume, which provides an effective and sustainable way toward large-scale wind energy harvesting in the future.

2. Results and Discussion

2.1. Structure and Working Mechanism of D-TENG

As shown in **Figure 1**a, the auto-switching wind energy harvesting system has a multilayered structure, mainly contains a wind energy collection module that consists of two sets of wind cups with varied arm lengths, and a double-TENGs module enclosed in a hermetic package. Figure 1b demonstrates the detailed structural view of the system for a better understanding. Herein, the wind energy collection module consists of two coaxial wind cups with different arm lengths, and each of them owns an independent rotation shaft. The wind cups used for harvesting wind will drive the double-TENG module by their dual-rotation shaft. The double-TENG module at the bottom consists of two concentric planar-structured TENGs, that is, the inner TENG (I-TENG) and the outer TENG (O-TENG), of which the I-TENG is connected with the inner rotator and the O-TENG is linked with the outer one. Both rotators with fluorinated ethylene propylene (FEP) film play as triboelectric surfaces. Specifically, the inner rotator is a collection of radially-arrayed sectors separated by equal-degree

**ADVANCED
SCIENCE NEWS**

www.advancedsciencenews.com
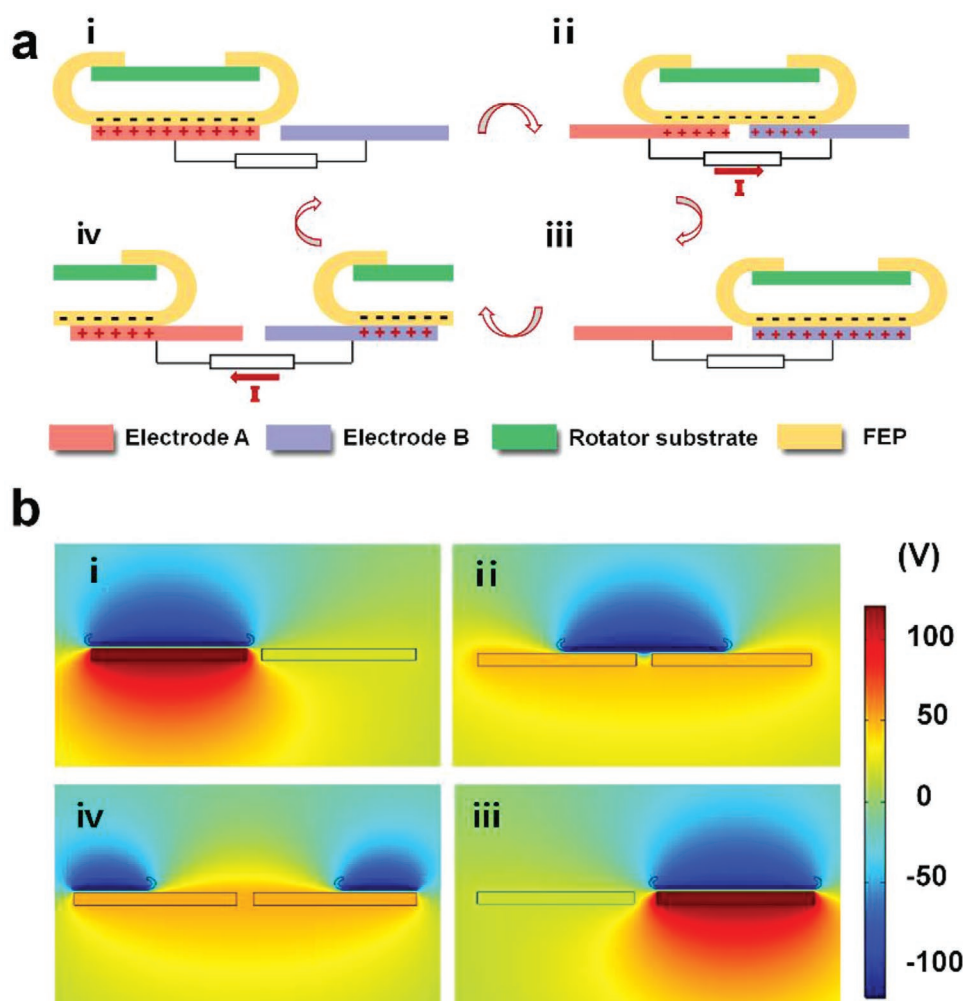
**ADVANCED
ENERGY
MATERIALS**

www.advenergymat.de

Figure 1. Structural design of the dual-rotation shaft TENG (D-TENG). a) Schematic illustration of the D-TENG, which is expanded in (b) that consists of the two wind-cup sets with dual-rotation shafts as the energy collection module, and double TENGs module constituted by the rotators with FEP films, and the bottom stator as the electrode. c) Enlarged photograph of rotor, whose edges were fixed with sides of FEP films, leaving the middle part of film slightly arched. d) Photograph of the D-TENG. e) Comparisons of SEM images for FEP film and copper film i,ii) before and iii, iv) after 3-month operation.

intervals in between, with a central angle of 15°, the rotator has a total of 6 units. While the outer rotator is an annular shape with three spokes connected to the center, on which the circular ring is separated into 12 units with a central angle of 15°, and every other unit is regarded as the sectors of the outer rotator. Each sector of two rotators is totally covered by a pie-shaped FEP film, with their two sides fixed at the edges of each sector, leaving the middle part of the film slightly arched. The arched part will be naturally bent and appropriately in contact with the stator. The two TENGs share the one stator, which is composed of two parts, that is, the inner part and outer part. And each part consists of two complementary-patterned electrode networks that are disconnected by fine trenches in between. Having the same pattern as that of each rotator, each network from two parts on the stator is formed by a radial array of sectors that are mutually connected at one end. As each adjacent network belongs to the opposite electrode, the two networks from each part can be regarded as two electrodes. In addition, the distance between the rotator and stator should be adjusted properly, making the arched part of FEP film completely contact only one network without covering the adjacent one, as shown in Figure 1c. As exhibited in Figure 1d, the device has the dimensions 28 cm × 28 cm × 23 cm (L × W × H). This dual-rotation shaft design not only leads to structural simplicity but also accounts for excellent portability. The scanning electron microscope (SEM) images of the FEP film and

Cu electrode are shown in Figure 1e, where the SEM images of original friction materials (Figure 1e i,ii) are compared with that after 3 months of repeated operations (Figure 1e iii,iv). Due to the introduction of the soft friction instead of the rigid one, the repeated relative friction hardly produces any major scratches on both surfaces of FEP film and Cu electrode, which implies an excellent wear resistance in the surface morphology. On the other hand, the Fourier transform infrared spectroscopy spectra of original and used FEP films were measured for a better illustration from the perspective of chemical groups. According to the molecular structure of FEP, the three fluorine groups "-CF-," "-CF$_2$-," and "-CF$_3$-" are the main roles to reflect the electronegativity that determines the output performance. As shown in Figure S1, Supporting Information, there is no distinct decrease in the peaks of the three fluorine groups between the FEP films before and after use, which implies the electronegativity can maintain the level, leading to the slight degradation of the device. In this regard, the minor variation in the chemical groups is due to the encapsulation, which prevents the environmental factors affecting the chemical properties of materials. Therefore, the output performances nearly maintain the same level (Figure S2, Supporting Information), demonstrating the preferable durability.

Figure 2a illustrates the electricity generation process under the relative rotation motions between the FEP films and the Cu

**ADVANCED
SCIENCE NEWS**
www.advancedsciencenews.com

**ADVANCED
ENERGY
MATERIALS**
www.advenergymat.de

Figure 2. Schematics of working mechanism of D-TENG in the soft friction mode. a: i–iv) Schematic charge distribution and current direction of the D-TENG in a whole cycle and b: i–v) Electric potential distributions at corresponding displacements by COMSOL employing the finite element method.

electrodes, through which alternating current is provided to the external load. Herein, we define the Cu electrode that first in complete contact with the FEP film is the electrode-A, and the electrode which is adjacent to the previous one is the electrode-B. In the initial state, the FEP film is in complete contact with the electrode-A, resulting in the generation of negative charge through the triboelectrification (Figure 2a,i). Consequently, the positive charge in the loop will be attracted to the upper surface of the electrode-A due to the electrostatic induction, making the positive charges on the electrode-A has the same amount with the negative ones on the FEP film. As the FEP film moves toward the electrode-B, the electrostatic inductive force will drive the positive charges in the loop to flow from the electrode-A to the electrode-B, generating a current flows via load from electrode-A to electrode-B (Figure 2a ii). Once the FEP film completely overlaps with the electrode-B, all the positive charges will be attracted to the upper surface of the electrode-B, which is regarded as the first half cycle of electricity generation. As the rotor keeps rotating, the FEP film will continue to move from the electrode-B to the next electrode-A, thus creating a reverse load current. By

the time when the FEP film fully contacts with the electrode-A, the whole cycle of electricity generation by TENG is finished.

According to the disk-shaped structure, the total transferred charge amount through TENG's fan-shaped electrodes per cycle can be expressed by Equation (1).

$$Q = \frac{a_0}{180} \cdot \pi \left(r_2^2 - r_1^2 \right) \cdot \sigma' \tag{1}$$

where a_0 is the central angle of each single electrode unit, which is 10°for I-TENG, and 20°for O-TENG. r_2 and r_1 represent the outer and inner radius of rotors, which are 0.095 and 0.025 m for the I-TENG, and 0.135 and 0.095 m for the O-TENG, respectively. σ' is the equivalent triboelectric charge density of the disk-shaped TENG, which is set as ≈100 µC·m^{-2} as it has only one triboelectric layer compared with the double triboelectric layers in Zhu's TENG.[39]

As the pole pairs of TENG can be defined as Equation (2).

$$p = \frac{180}{a_0} \tag{2}$$

**ADVANCED
SCIENCE NEWS**
www.advancedsciencenews.com

**ADVANCED
ENERGY
MATERIALS**
www.advenergymat.de

Thus the total amount of the transferred charge for each TENG can be calculated from Equations (1) and (2) can be further expressed as Equation (3).

$$Q = \frac{\sigma'}{p} \cdot \frac{\pi(r_2^2 - r_1^2)}{2} = \frac{\sigma' \cdot S_f}{p} \tag{3}$$

where S_f is the friction area of each TENG, which is estimated as 0.013 and 0.014 m^2 for I-TENG and O-TENG respectively. Based on Equations (1)–(3), the transferred charge of I-TENG and O-TENG is theoretically estimated to be 147 and 321 nC, respectively. The above charges are transferred periodically through electrodes generating the alternating current with a frequency of Equation (4).

$$f = \frac{180v}{a_0} = vp \tag{4}$$

In the open-circuit condition, since the charges cannot transfer between electrodes without load, the charges between the electrodes will generate a periodic potential difference between the two electrodes by the effect of electrostatic screening. Herein, the open-circuit voltage (V_{oc}) is defined as the electric potential difference between the two electrodes, and the electrostatic induction process can produce V_{oc} signals as the positive charges on the electrode orderly screened by the negative triboelectric charges on the FEP film. In this way, the V_{oc} reaches its maximum value as one of the electrodes is fully covered by the FEP film, as shown in the inset of Figure 2a i,iii. Such a voltage then decreases as the rotator rotates. Once the rotor moves to the middle position of the two electrodes, the potential difference is zero for the equal amount of induced charges on both surfaces, and the V_{oc} value reaches the zero-crossing point then starts to accumulate the reverse potential difference until the rotor rotates to the next middle position (Figure 2a ii,iv). For further understanding, the continuous variation of the V_{oc} is visualized through finite-element simulation using COMSOL, as shown in Figure 2b.

2.2. The Output and Characteristics of D-TENG

To characterize the electrical output performance of the D-TENG, a wind turbine system with adjustable wind speed controlled by applied voltage (Figure S3, Supporting Information) is established to simulate the wind energy, with the wind speed range of 0–16 m s^{-1}. By measuring the open-circuit voltage (V_{oc}), short-circuit current (I_{sc}), and transferred charge quantity (Q_{sc}) of the O-TENG and I-TENG at different wind speeds, the signals of V_{oc}, I_{sc}, and Q_{sc} for variable wind speeds were obtained as shown in **Figure 3**a–f. Specifically, for the I-TENG as seen in Figure 3a–c, V_{oc} and Q_{sc} exhibit an uptrend in the low speed range (2.2–5.4 m s^{-1}) then remains almost constant value of 200 V and 130 nC with wind speed increased from 2.2 to 16.2 m s^{-1}, while I_{sc} shows a positively proportional relationship with wind speed during the whole range, with the initial value of 4.3 μA to the maximum value of 19 μA. Figure 3d–f shows the variations of V_{oc}, I_{sc}, and Q_{sc} for the O-TENG under the same wind-driven system. Compared with the I-TENG, the

O-TENG requires a higher start-up wind speed with the relevant signals appear at the wind speed of 5.4 m s^{-1}. The trends of these signals for O-TENG are similar to that for I-TENG except for the starting points, however the amplitudes of signals for O-TENG are more dominant. The maintained values for V_{oc} and Q_{sc} from O-TENG are 300 V and 200 nC, which are nearly 50% higher than that from I-TENG. The enhanced voltage and charges will have an active effect on the current, whose maximum value has been increased to 32 μA, reaching nearly two times the amplitude of current in I-TENG.

The reason that V_{oc} and Q_{sc} first climb then remain essentially constant in the stable operation phase is for the working principle of freestanding mode of soft-friction TENG. In the start-up operation phase, the FEP film of TENG is not entirely extended due to the gravitational deformation, causing the inadequate contact with the bottom electrode, which results in a less amount of charges generated from triboelectrification. As the wind speed accelerates, the buoyancy caused by the air flow will partly balance the gravity, making the FEP film fully contact the electrode under the stretched state. The triboelectric charges will accordingly increase to the saturated amount of transferred charge. In the stable operation, each of the I-TENG and O-TENG can be considered as a capacitor transferring constant charges through two electrodes, and its terminal voltage is denoted as Equation (5).

$$U = \frac{dQ}{dC} \tag{5}$$

where Q is the transferred charge between the TENG electrodes and C denotes the equivalent capacitance of each TENG. Since the equivalent capacitance of the TENG is only related to its material properties (σ) and shape dimensions (r_1, r_2), the V_{oc} is directly related to the charge transfer between the two electrodes and its transferred charge quantity (Q_{sc}) is represented by Equation (1), implying that Q_{sc} also depends on the properties of the friction material and the shape and size parameters of the TENG. Therefore, V_{oc} and Q_{sc} keep basically constant under the growth of wind speed.

However, the I_{sc} varies almost linearly versus wind speed, which is regarded as a core advantage of freestanding mode of TENG. Since the current is defined as the rate of charge transfer, as shown in Equation (6).

$$I = \frac{dQ}{dt} \tag{6}$$

Then the average current (I_{av}) of the TENG over half a cycle is calculated from Equations (1) and (4) as Equation (7).

$$I_{av} = Q / \frac{T}{2} = 2Qf = \sigma\pi\left(r_2^2 - r_1^2\right)vp / 2 \tag{7}$$

Thus the increase of wind speed accelerates the rotation speed (v) of TENG, which results in a faster transfer of a fixed amount of charge (Q) between the electrodes, resulting in a larger current. Once the load is connected, the load voltage, load current, and instantaneous output power can be obtained. Here, we take I-TENG for example. The load characteristics for
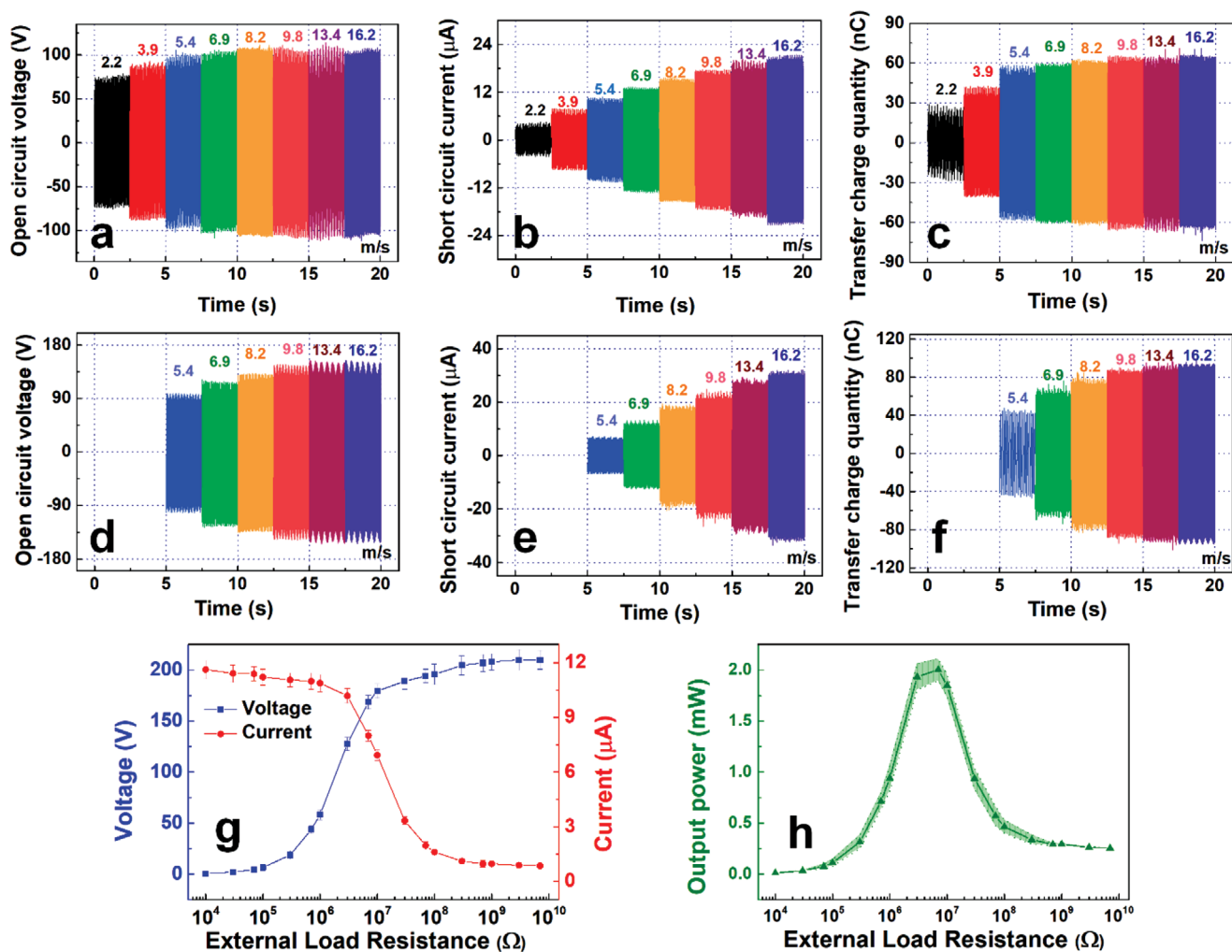
Figure 3. Electrical measurements of the D-TENG. a) V_{oc}, c) I_{sc}, and e) Q_{sc} of the I-TENG under typical wind speeds. b) V_{oc}, d) I_{sc}, and f) Q_{sc} of the O-TENG under typical wind speeds. g) Amplitudes of output voltage and current of I-TENG under varied external load resistances at 6 m s^{-1} wind speed. h) Dependences of output peak power for I-TENG on varied resistive loads 6 m s^{-1} wind speed.

I-TENG driven under 6 m s^{-1} were collected in Figure 3g,h. The amplitude of the output current drops as the load impedance increases, while that of output voltage appears a reverse trend. The instantaneous output power for I-TENG is maximized at a load resistance of 7 MΩ, corresponding to a peak power of 2.0 mW.

2.3. Structural Optimization

A favorable TENG-based wind system requires not only a good aerodynamic performance for its energy collection module, but also a satisfactory conversion efficiency for its TENG part. The arm length in the energy collection module is closely related to the dynamic performance, and also has an effect on the conversion efficiency through the rational speed. Theoretically, there exists a corresponding arm length of the wind cup that can both maximize the current kinetic performance and efficiency under any particular speed. Therefore, if the arm length could

be adjusted in the real time to adapt to different wind conditions, the maximum efficiency can be generated under the good dynamic performance. However, such an intelligent design of this structure is a complicated goal that requires many factors to be considered, which might lead to the cost increment and the reliability reduction. An alternative way is to integrate the wind cups of different arm lengths into a single unit, that is, a multistage structure. Through the optimizations of the wind cups and the corresponding TENG designs, this structure is able to automatically switch at different wind speeds, thus improving the aerodynamic performance and the conversion efficiency at each wind speed. Ideally, a multiple switched stage represents more subdivisions that result in a more conversion efficiency. However, since each stage works independently for each other, thus an excessive number of stages will bring out the difficulties in fabrication and the reliability reduction in operation. Therefore, in order to facilitate the fabrication, research, and discussion, a simple dual-stage structure was selected, and the related parameters were discovered in this section.
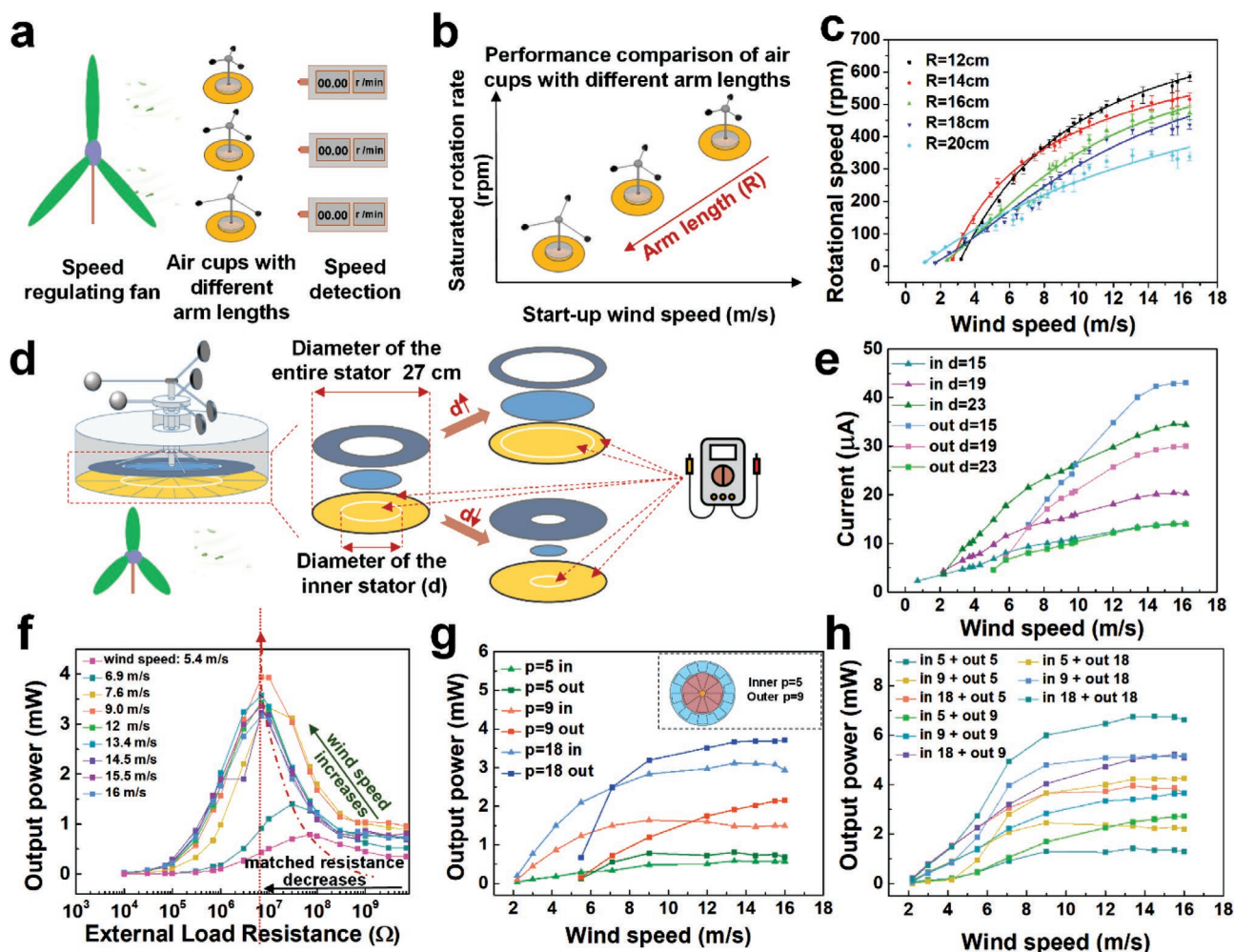
Figure 4. Structural parameters optimization of D-TENG. a) Schematic diagram of aerodynamic tests for wind cups with different arm lengths. b) Schematic diagram of relationships between the saturated rotation rate versus the start-up wind speed for the different arm lengths. c) Measured relationship between the rotational speed and wind speed of wind cups with varied arm lengths. d) Schematic diagram of the electrical measurements for I-TENG and O-TENG under different sizes with the entire stator and inner stator marked on it, and e) curves of current variation with wind speed for each size of TENG. f) Curves of output power with load for O-TENG under different wind speeds. g) Output power variation curves of different pole-pairs for both TENGs with varied wind speeds, the schematic diagram of pole-pairs displayed at the top left corner. h) Power variation curves with wind speed for I-TENG and O-TENG output together with different pole pairs under varied wind speed.

2.3.1. Optimization of Aerodynamic Performance

The wind cups, as the energy collection module of D-TENG, play vital roles in the aerodynamic performance of the whole system. Since the D-TENG has two complementary parts, the aerodynamic performance not only means the kinetic response performance of each TENG, but also contains the dynamic coordination of both TENGs. In order to explore the aerodynamic performance, five wind cups with different arm lengths ranging from 12 to 20 cm with an interval of 2 cm were experimentally fabricated (Figure S4, Supporting Information). As shown in **Figure 4**a, the rotation rate of each wind cup at different wind speeds was measured separately by a non-contact laser speed sensor, and the characteristics and results are shown in Figure 4b–c. Figure 4b exhibits an inverse linear relationship between the start-up speed and the saturation speed as the arm length increases, which indicates the contradiction dilemma on

the start-up and saturation speeds for any certain arm length. Therefore, it would be beneficial to select two kinds of arm lengths to achieve the mutual complementation. The small arm length shows higher start-up speed and saturation speed, which can be compensated by the long arm length for its lower start-up speed. The reason for the different start-up speeds and saturation speeds varied by the arm lengths is attributed to the torques. For any fixed-size wind cup, the driving force (F) provided by the wind energy is a function of the wind speed (v) and the air density (ρ), as expressed by Equation (8).

$$\vec{F} = f(\vec{v}, \rho) \tag{8}$$

then the torque (M) on the wind cup driven by the force is given by Equation (9).

$$\vec{M} = \vec{F} \times \vec{L} \tag{9}$$

ADVANCED
SCIENCE NEWS
www.advancedsciencenews.com

ADVANCED
ENERGY
MATERIALS
www.advenergymat.de

where L is the arm length of the wind cup. The start-up speed here can be regarded as the initial torque (M_0) to overcome the friction between the triboelectric layer and electrodes of TENG, whose relation to the required start-up wind speed (v_0) can be expressed in Equation (10).

$$\vec{M}_0 = f(\vec{v}_0, \rho) \times \vec{L} \tag{10}$$

based on Equation (10), as the minimum torque M_0 required to drive the wind cup stays constant, the start-up speed (v_0) presents an inverse correlation with the arm length (L). However, the rotational speed of the wind cup (ω) also exhibits reciprocal relation with the arm length under the same linear velocity speed, which equals the current wind speed (v_0), as shown in Equation (11).

$$v = \omega L \tag{11}$$

which indicates that the wind cup with long arm length has a lower rotational speed under the same driving force. More importantly, since the output voltage of TENG is essentially stable with wind speed, and the output current is proportional to the rotational speed, thus a relatively long arm length will inevitably reduce the energy conversion efficiency of the TENG. On the contrary, to enhance the energy conversion efficiency of TENG, the arm length of the wind cup needs to be minimized, which will reduce the torque and thus increase the start-up wind speed, disabling the applicability in the breeze energy. Therefore, an alternative way that making the long and short arm length work together is an effective way to broaden the operating range of wind energy harvesting devices.

Besides the start-up and saturation wind speeds, the switching wind speed for both wind cups with varied arm lengths should also be considered as the most important criteria for the nice dynamic coordination. If the switching wind speed is set too high, it will hard to launch the wind cup with short arm length and result in an energy waste. Inversely, a lower switching wind speed will reduce the saturation speed to reduce the efficiency. Figure 4c records the rational speed curves for each wind cup with different arm lengths under varied wind speed. The wind cup with radius of 20 cm has the best start-up wind speed (1.2 m s^{-1}), and that of 12 cm owns the best saturation rotation speed (578 rpm). However, the switching wind speed of these two wind cups is ≈4.5 m s^{-1}, which belongs to the moderate wind. By comparison, the wind cup with radius of 14 cm can be combined with that of 20 cm, with a switching wind speed of 3.6 m s^{-1}, which belongs to the breeze wind. Although the wind cup with 12 cm radius owns the prime saturation speed, the corresponding wind speed is over 12 m s^{-1}, which is rare in our daily life. In this regard, two types of wind cups with arm lengths of 20 and 14 cm were selected for the I-TENG and O-TENG respectively.

2.3.2. Optimization of TENG Size

The size of TENG has a positive effect on its output electrical signal, which is characterized by Equations (1) and (7), implying that a larger friction area can generate higher value in its Q_{sc}

and I_{sc}. However, the larger friction area means the enhanced start-up torque, which will bring difficulties in the TENG operation, as expressed in Equation (12):

$$\vec{M}_t = \vec{M}_a + \vec{M}_f + \vec{M}_e \tag{12}$$

where M_a is the resistance torque from the rotation of the bearing. M_f is the resistance torque from the friction between the FEP film and the electrodes, and M_e is the resistance torque by electrostatic force from the charges carried by the FEP film and electrodes. Both M_f and M_e are proportional to the TENG friction area, leading to the difficulties in the TENG launch. Since the I-TENG and the O-TENG in the D-TENG have different tasks, aiming to the low start-up and high rotational speed reactively. Therefore, the sizes of I-TENG and O-TENG in the planar area need to be considered for a better driving force by wind cups. Figure 4d and Figure S5, Supporting Information illustrate the scheme of TENG size optimization. The total outer diameter of the D-TENG is fixed at 27 cm, which is also the outer diameter of the O-TENG. The outer diameter of I-TENG is set at 15, 19, and 23 cm, respectively, thus the inner diameter of O-TENG will gradually increase from 15 to 23 cm. The friction area of each TENG is calculated as Equations (13) and (14).

$$S_{I-TENG} = \pi \left(\frac{d^2}{4} - \frac{d_0^2}{4} \right) / 2 \tag{13}$$

$$S_{O-TENG} = \pi \left(\frac{D^2}{4} - \frac{d^2}{4} \right) / 2 \tag{14}$$

where D (0.27 m) is the outer diameter of the O-TENG, d_0 (0.05 m) is the inner diameter of the I-TENG, and d is the outer diameter of the I-TENG, or the inner diameter of the O-TENG. Since the voltage value of the D-TENG basically stays constant at different wind speeds, the current value is selected to characterize the output performance. Figure 4e shows variation of I_{sc} for three sets of I-TENG and O-TENG with varied diameters at different wind speeds. Overall speaking, as demonstrated in Figure 4e and Movie S1, Supporting Information, the I_{sc} of I-TENG starts to appear at the wind speed of 1 m s^{-1}, and its amplitude ranges from 0–30 μA, while that of O-TENG starts when the wind speed increases to ≈5 m s^{-1}, but the curve rises rapidly than that of the I-TENG, with its maximum value of 44.3 μA. As the d of I-TENG increases, the S_{I-TENG} increases correspondingly, leading to the enhancement of I_{sc} at the cost of start-up wind speed. The O-TENG however shows the opposite trend with I-TENG, that is, the larger d is, the smaller S_{O-TENG} would be, corresponding to a smaller I_{sc} and a lower start-up wind speed. When d is relatively small (e.g., 15 cm), the I-TENG can be activated at the wind speed of 1 m s^{-1}, but its output current grows gently and approaches 10 μA at the wind speed of 8 m s^{-1}, the corresponding O-TENG needs to start at the speed of 7 m s^{-1}. When d is relatively large (e.g., 23 cm), the I-TENG starts at ≈2 m s^{-1} wind speed with a larger I_{sc}, but the I_{sc} of the corresponding O-TENG is lower, whose value is comparable to that of I-TENG over the entire wind speed range, thus there is no complementary relationship between the I-TENG and the

O-TENG. The favorable size for both TENG is the middle size (e.g., 19 cm), with which the I-TENG starts at ≈2 m s⁻¹ and its output current rises to 10 µA between 5 and 6 m s⁻¹, while for the O-TENG, the current curve starts rapidly and the rising rate exceeds that of the I-TENG by nearly two times, presenting a higher maximum current value.

Furthermore, within the determined sizes of both TENG, the maximum output power (P_m) combined with the corresponding matching impedance (R_m) were also discovered with a series of varied loads under different wind speeds, with the results for O-TENG displaying in Figure 4f and that for I-TENG displaying in Figure S6, Supporting Information. The curves for both TENG experience the similar trend, here we only take O-TENG for example. At the start-up wind speed, the corresponding R_m of O-TENG is 30 MΩ, and P_m of that is only 1.4 mW. As the wind speed increases, the R_m gradually becomes smaller and stabilizes around 3 MΩ, while the P_m reaches at a maximum of 3.9 mW around 9 m s⁻¹, after which the P_m decreases slightly and stabilizes around 3 mW.

2.3.3. Optimization of TENG Pole-Pairs

For any kinds of disk-shaped TENGs, once the structural parameters are basically determined (that is, r_1 and r_2 keep unchanged), the equivalent capacitance of the TENG is basically fixed, therefore the Q_{sc} and V_{oc} are basically constant, and I_{sc} would be the only variable influenced by the number of pole pairs (p) according to Equation (6). The number of pole pairs refers to the number of vanes in TENG rotator, and also refers to the number of electrodes in single network in TENG stator, which means the TENG outputs p periods of AC output per rotation for one circle. The p with a relatively higher value could enhance the current output by raising the charge transfer rate, which can improve the output power of the whole system. However, the value of p cannot be raised all the time. In practice, not only is it difficult to fabricate too many pairs of poles, but the increment in p also makes the rotator of TENG fragile and brittle. Moreover, the excessive number of pole-pairs cannot keep the current rising continuously, but cause the decrement in the voltage, current, and transferred charges. This is because that too many pairs of poles will reduce the area of single electrode, making the adjacent electrodes too close with each other, which in turn will screen the charges between adjacent electrodes based on the electrostatic induction, thus greatly cut down the amount of transferred charges between the electrodes.
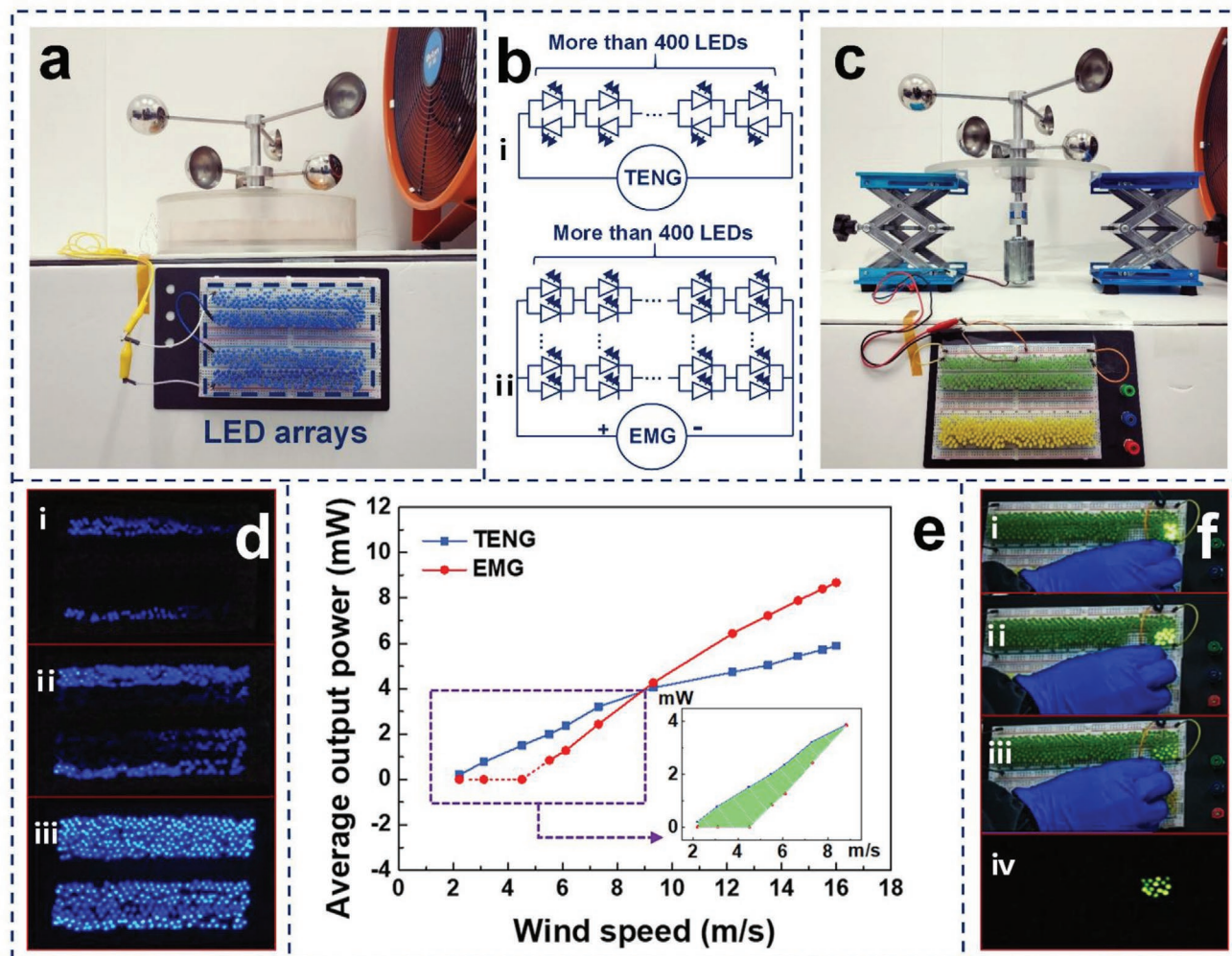
In order to verify the effect of p on the output power of both TENGs, a total of six units for I-TENG and O-TENG with its p sets at 5, 9, and 18 were respectively fabricated as displayed in Figure S7, Supporting Information. Figure 4g shows the power curves of each TENG unit under the 3 MΩ resistant load at different wind speeds, and Figure 4h exhibits the curves of total output power by cross combinations versus the varied wind speeds. In Figure 4g, the I-TENG starts promptly at ≈2 m s⁻¹, and its output power increases linearly with the wind speed in the early stage. As the wind speed reaches 6 m s⁻¹, the power curve finally tends to saturate and stabilizes at a certain value or decreases slightly. On the other hand, the O-TENG starts at wind speed around 5 m s⁻¹ and its output power first rises

rapidly and overtakes the I-TENG around 6 m s⁻¹. After that, the output power of O-TENG continues to grow at a slower rate and finally stabilizes in a certain range. It is easily observed that the output powers for both I-TENG and O-TENG are positively correlated with the pole pairs in a basically linear relationship. In the practical operation of D-TENG, only the I-TENG can start and collect the wind energy under the breeze, while the O-TENG will start in the wind speed around 4–6 m s⁻¹, after which the I-TENG will collect the wind energy together with the O-TENG to supply the electric power cooperatively, thus the output power is the superposition of both values. When the O-TENG joins in the operation of the I-TENG, the total output power will be suddenly raised, which would be adverse on the rear circuit. Therefore, in order to make the power change smoother at the switching moment between I-TENG and O-TENG, a favorable combination of I-TENG and O-TENG (in 18 + out 9) with the largest output power and the smoothest power curve is selected among many power curves in Figure 4h, in which the start-up wind speed is only 2.2 m s⁻¹, and the maximum output power reaches 5.2 mW.

2.4. Energy Output Capability of D-TENG

To further explore the overall energy output capability for D-TENG, the average output powers over a broad wind speed range were collected and calculated by connecting to external loads through a rectifier. Meanwhile, an EMG with the same wind harvesting structure was introduced for a better comparison. Notably, the two wind-cup structures were integrated together through a simple differential module making the EMG be driven under one set of wind-cup which owns higher rotation speed. The array of light emitting diodes (LEDs) were employed as the external load for the visual comparison, of which, 400 blue LEDs were connected in series, and green LEDs with same number were in parallel connection. **Figure 5**a,c displays the measurement platforms for D-TENG and EMG installed with the same wind-cup combinations under the wind turbine system. Figure 5b illustrates the circuit diagrams for the two generators. In the process of D-TENG operation, I-TENG will start first and O-TENG subsequently join to work together to drive the LEDs under the increased wind speed, with the results of varied brightness of LEDs under the corresponding wind speed displayed in Figure 5d i–iii and Movie S2, Supporting Information. It is clearly observed that when the wind speed is low (around 2 m s⁻¹), the total power was provided by I-TENG alone. Although the power output is limited, it can drive nearly half of the total LEDs. Once the wind speed reaches ≈6 m s⁻¹, the O-TENG starts to launch and a majority number of LEDs were lighted only by the output of O-TENG. By connecting the I-TENG and O-TENG in series to make them work together under the same wind speed, more than 400 LEDs were illuminated with significantly higher brightness.

The different brightness of LEDs in EMG operation as the wind speed ranged the situation with that in D-TENG were also investigated. As demonstrated in Movie S3, Supporting Information, the EMG starts to operate when the wind speed reaches 5 m s⁻¹, at which the O-TENG will about to launch in the D-TENG. At this point, the output of EMG is difficult to

ADVANCED
SCIENCE NEWS
www.advancedsciencenews.com

ADVANCED
ENERGY
MATERIALS
www.advenergymat.de

Figure 5. Overall energy output capabilities for D-TENG and EMG. Photographs of experimental platform of a) D-TENG and c) EMG with the same energy harvesting structure driving LED array independently with b) their connection diagrams. d) The brightness demonstration of LED array driven by I-TENG and O-TENG at the wind speed of i) 4.5 m s⁻¹, ii) 6 m s⁻¹, and iii) 7 m s⁻¹. e) The average output powers for both D-TENG and EMG under the whole wind speed range with LED load. f) The brightness demonstration of LED array driven by EMG at a wind speed of 7 m s⁻¹ with the number of LEDs at i) 6, ii) 12, iii,iv) 14.

drive the whole LEDs even the speed is increased to the 6 m s⁻¹, which is the same comparable speed with D-TENG. Therefore, LEDs were individually connected in experiments as displayed in Figure 5f i–iv and Movie S4, Supporting Information. As a small number of LEDs connected in load, the LEDs seem bright due to the high output current (mA level), however, when the number of connected LEDs gradually increases, the brightness of LEDs diminishes significantly. Once roughly 20 LEDs were connected, the load capacity of EMG at this wind speed has reached its limit to drive more LEDs. The reason for the disparate load capacity for EMG is due to its own feature. For EMGs, the induced electric potential V_{oc} is denoted as Equation (15):

$$V_{oc} = -N\frac{d\varphi}{dt} = -NS\frac{dB(x)}{dt} = -NS\frac{dB(x)/dx}{dx/dt} = -NS\frac{dB(x)}{dx}\cdot v \quad (15)$$

where N is the number of coil turns, Φ is the total magnetic flux in a coil, $B(x)$ is the magnetic induction intensity, S is the

area of the coil, and v is the speed of coil motion. Thus, the I_{sc} of EMG is expressed as Equation (16).

$$I_{sc} = \frac{V_{oc}}{R_{coil}} = -\frac{NS}{R_{coil}}\cdot\frac{dB(x)}{dx}\cdot v \quad (16)$$

where R_{coil} is the resistance of the coil. In this feature, as the ambient wind speed changes repeatedly, the rotor speed (v) of the EMG changes, making both V_{oc} and I_{sc} of EMG changed accordingly, thus affect the output stability on load. Moreover, due to its inherent ferromagnetic coil structure, the mass of the EMG with same volume is several times than that of the TENG, making it difficult to be driven under the low-speed wind. If the EMG is made less heavy to satisfy the breeze condition, the size will be largely reduced, thus inevitably reduce the output power.

To quantitatively characterize the load capabilities of D-TENG and EMG under loads over a wider wind speed range, the average output powers of D-TENG and EMG were obtained
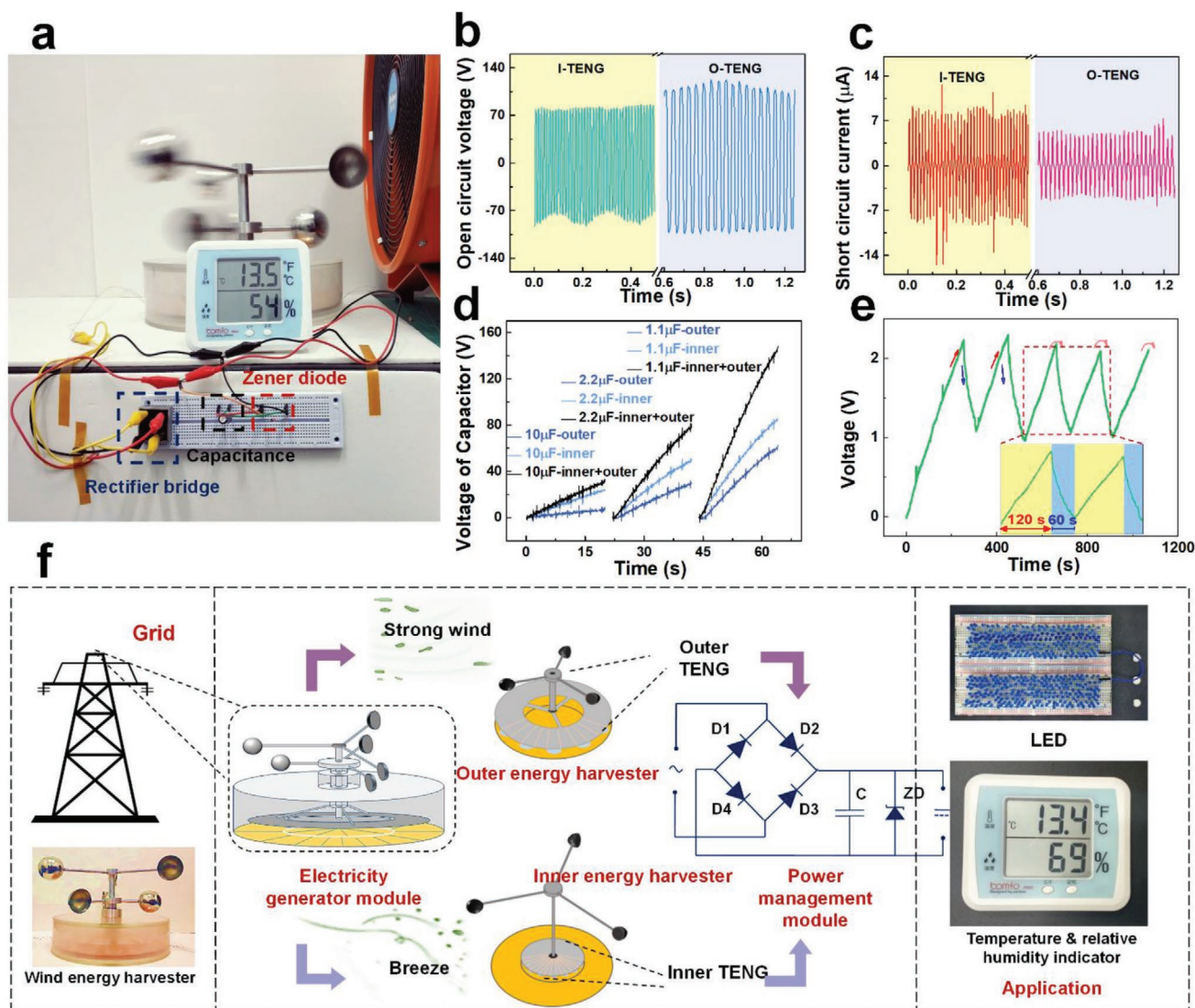
Figure 6. Demonstration of the D-TENG as a practical power source. a) Photograph of the D-TENG based self-powered system connected with thermometer by a rectifier and a capacitance under the wind turbine system. Electric measurements such as b) V_{oc}, and c) I_{sc}, of I-TENG and O-TENG were obtained at the wind speed of 6 m s^{-1}. d) Charging curves of I-TENG and O-TENG for varied capacitors at the wind speed of 6 m s^{-1}. e) Charge-discharge curve of the 1 mF capacitor during energy supply at the wind speed of 6 m s^{-1}, with its enlarged waveforms of two charge-discharge cycles shown in the inset below. f) Schematic diagram of workflow for the D-TENG based self-powered system.

over the wind speed ranged from 0 to 16 m s^{-1}, as shown in Figure 5e. With the increased wind speed, the average output power for D-TENG increases rapidly, while the growth rate for EMG rises slightly, the two curves thus intersected at a wind speed of 8.8 m s^{-1}. At this point, the D-TENG produces 3.9 mW more power than that of EMG by assuming the wind speed increased at a constant rate (rise speed: 0.1 m s^{-1} h^{-1}). Although the EMG can generate more output power as the wind speed over the intersection, the wind speed is relatively rare in our daily life. On the other hand, the energy conversion efficiencies for both TENG and EMG under the whole wind speed range were approximately calculated and plotted in Figure S8, Supporting Information. The D-TENG can provide 36–67% the energy conversion efficiency, which is two to four times the maximum efficiency that the EMG can convert. In

this regard, the D-TENG based on the lightweight friction and the dual-rotation shaft design enabled itself easily starting and steadily capturing the wind energy in breeze conditions as low as 2.2 m s^{-1}, thus greatly improving the harvesting range and efficiency in the wind energy collection.

2.5. Demonstration

To demonstrate the performance of D-TENG for wind energy harvesting, the device was fully packaged in an acrylic shell to avoid the soft films being affected by the wind disturbance. **Figure 6**a demonstrates the wind energy self-powered system that includes the D-TENG, an energy-stored capacitor, an energy management circuit as well as a commercial

thermometer. The self-powered system was operated under the wind speed of 6 m s^{-1}, at which both I-TENG and O-TENG can work properly. As shown in Figure 6b,c, an open-circuit voltage (V_{oc}) of 175 V and maximum short-circuit current (I_{sc}) of 9.2 μA have been reached for I-TENG, while the O-TENG can output a V_{oc} of 225 V, and an I_{sc} of 5.5 μA. The current amplitudes for both TENGs basically stay at the identical level due to the same stimulus, however the frequencies were varied for their poles of pairs, leading to the different average output powers. To stabilize the load voltage, a zener diode is connected in parallel with the capacitor for limiting the voltage at sensor terminals. The charging characteristics for D-TENG with different capacitors were obtained and plotted in Figure 6d. Both I-TENG and O-TENG can work independently and collaboratively by the linear superposition of their output voltages. As the capacitor is charged by D-TENG through a rectifier bridge, the voltage of the capacitor can be raised up to the V_{oc} of the TENG (around 200 V). The charging rate of the capacitor voltage is positively related to the instantaneous output power of the TENG and negatively related to its capacitance. Due to the constant amount of transferred charge per cycle, the TENG can essentially be viewed as a constant charge source, and the law of charging the capacitor is denoted as Equation (17).

$$C = \frac{dU_c}{dQ} = \frac{dU_c/dt}{dQ/dt} \tag{17}$$

where C is the capacitance, U_c is the capacitor voltage, and Q represents the charge on the capacitor electrodes. When the U_c is small, the increment of Q at each cycle is approximately equal (=Q_{sc}), so the dQ/dt is relatively fixed at the same wind speed, which means that the capacitor voltage U_c increases linearly with charging time. As the capacitor voltage continues to rise to approach the U_{oc}, the TENG no longer charges the capacitor, and the U_c gradually reaches saturation. Thus the curves finally tend to be saturated. Notably, under the wind speed of 6 m s^{-1}, the I-TENG designed for the low wind speed range operates in a nearly saturation state, while the O-TENG designed for the high range just activates, leading to a temporary lower output power at this wind speed, which causes the slower capacitor charging rate than that of the I-TENG. Once the thermometer is connected in load, the charged capacitor will be responsible for the power supply by transferring the charges to the sensor. As demonstrated in Figure 6a and Movie S5, Supporting Information, the capacitor with 1 mF was employed for the energy storage for a better driving property. In operation, the D-TENG is able to drive the thermometer continuously for 1 min after every 2 min charging under the wind speed of 6 m s^{-1}. As shown in Figure 6e, in the first operating cycle, the initial capacitor voltage (U_{C0}) is 0 V, which takes 4 min of continuous charging by the D-TENG. As the U_C rises to ≈2 V, the thermometer was turned on to continuously monitor the ambient temperature and humidity, during which the load current starts to appear and decays gradually in the discharging process of capacitor.

With such a stable ability of power generation, the D-TENG is also feasibly capable of being integrated with other application modules, and assembling to a self-powered system in the addition of energy storage module and management circuit.

The D-TENG based self-powered system is mostly installed on the high-altitude sites, like the power transmission tower, communication tower, and street lamps. Figure 6f demonstrates the workflow of the packaged self-powered sensing system, in which the D-TENG consists of I-TENG and D-TENG plays the key part for adapting to the varied ambient conditions. Specifically, the low-speed wind energy harvester can only drive the I-TENG, while the O-TENG is suitable for the high-speed wind energy. Under the normal breeze conditions, although the O-TENG hardly operates, the I-TENG is able to quickly respond and continuously collect these breeze energy, then intermittently power the electric applications. While in the strong winds, both TENGs will operate simultaneously, while the O-TENG will play a leading role with the higher conversion efficiency. In this way, the two TENGs can be mutual compensated for their own merits, enabling the whole system to deliver satisfactory output over a broad range of wind speeds. Benefiting from the favorable environmental adaptability, the self-powered sensing system exhibits great potential for application in more common environments with a higher energy capture efficiency.

3. Conclusion

In summary, an auto-switching self-powered system based on TENG has been proposed and fabricated for efficient wind energy harvesting. The TENG is designed in a concentric dual-rotation shaft structure, in which two independent TENGs with varied shapes, sizes, and arm lengths of wind cups are integrated for realizing the multi-stage energy harvesting function. Through the reasonable structural parameter design, the two TENG can start to operate successively any manual shifts. The two TENGs with mutual complementary aerodynamics and output performance enable the self-powered system to harvest wind energy and deliver satisfactory output in a broad range of wind speed, which is also regarded as a better solution to settle down the dilemma between the low start-up wind and high energy conversion efficiency. The device with varied arm lengths, radiuses, and pole-pairs were experimentally determined by comparing the aerodynamics and output performances of optional designs. In the perspectives of well output capability and favorable coordination, the arm length of wind cups for I-TENG is set 20 cm and the number of pole-pairs is 18, while that for O-TENG are 14 cm and 9, respectively. The diameter of the entire stator is 27 cm, while a better diameter for the inner stator is 19 cm for the D-TENG. With these particular design parameters, the system can effectively collect wind energy with the speeds ranged from 2.2 to 16 m s^{-1}, in which the start-up wind speed is only 2.2 m s^{-1} considering the overall dimension, and the switching wind speed is ≈5–6 m s^{-1}. The overall output performance depends on the respective output performances for both TENGs, the I-TENG can output a V_{oc} of 228 V and an I_{sc} of 18.9 μA, while a V_{oc} of 306 V and an I_{sc} of 32 μA has been achieved for the O-TENG. The output powers for I-TENG is 2.0 mW at the matched impedance of 7 MΩ under the wind speed of 6 m s^{-1}. Moreover, an EMG with the same wind harvesting structure was introduced for a better comparison through the average output power measurements and brightness display of LEDs. As a result, the fabricated

D-TENG owns excellent launching property, and its output power as well as conversion efficiency is superior to the EMG in the wind speed range of 2.2–8.6 m s^{-1}. Finally, the packaged self-powered system was demonstrated to harvest simulated wind energy to drive a thermometer through a rectifying circuit. With the multi-stage structure, the D-TENG renders an effective and progress in the practical applications of large-scale wind energy harvesting over a broad frequency range.

4. Experimental Section

Fabrication of the Dual-Rotation Shaft Wind Energy Harvesting System: From Figure 1b, the fabricated wind energy harvesting system consists of three main components, that is, from top to bottom, the wind energy collection module that consists of two sets of wind cups with varied arm lengths, the rotors of both I-TENG and O-TENG, and their stators that integrate on a single acrylic disc.

For the Wind Energy Collection Module Fabrication: An aluminum rotation shaft with a length of 10 cm and a diameter of 3.2 cm was machined into a hollow structure so that another solid aluminum shaft with a length of 20 cm and the diameter of 1.8 cm could be fixed inside the hollow one by insulated bearings, thus forming a concentric dual-rotation shaft structure in which each of the shafts could rotate independently. Then, three hollow hemispherical aluminum cups with a diameter of 6 cm were fixed to one end of three aluminum brackets with a diameter of 0.8 cm, respectively, while the other end of the brackets was fixed to the top of the solid spindle so that a wind cup with a radius of 20 cm was formed. Another wind cup of 14 cm radius was also been made by fixed three aluminum cups of the same size above to three slightly shorter aluminum brackets of 0.8 cm diameter at one end, while the other end was attached to the top of the hollow spindle. These two concentric dual-rotation shaft wind cups of different sizes were installed on the upper surface of the insulating package of D-TENG by a bearing connection, and the rotator of I-TENG was fixed at the bottom of the solid shaft while the rotator of O-TENG was fixed at the bottom of the hollow rotor, so that the two rotors can be suspended at a certain distance directly above the stator.

For the Rotor of D-TENG Fabrication: A 100 μm thick FEP film was cut into a fan shape to serve as a dielectric layer, also called the friction layer, and subsequently slid against the surface of the Cu film to collect charge. A 0.2 cm thick acrylic sheet was cut by a laser cutter (Universal Laser System) into a radial shaped disc with a diameter of 19 cm, that is, the rotator substrate of I-TENG, with a central angle of 20° for each fan-shaped sector. Then, an acrylic sheet of the same thickness was cut by laser cutting technique into an annular-shaped rotator with an outer diameter of 27 cm and an inner diameter of 19 cm, and was connected to the center by three spokes to serve as the rotator substrate of O-TENG, whose circle was divided equally into 36 sectors with a central angle of 10° for each. The ends of FEP films were fixed to the ends of sectors of I-TENG and to the ends of the alternate sectors of O-TENG so that their middle parts were slightly arched and in contact with the stator.

For the Stator of D-TENG Fabrication: A 0.2 cm thick acrylic sheet was cut by a laser cutter into a disc shape with a diameter of 27 cm to serve as the common stator substrate for both I-TENG and O-TENG. Copper foil was employed to adhere on the upper surface of the stator substrate as the electrode and friction material for D-TENG, and a circle etched trench was incised at a distance of 9.5 cm to the center to divide the foil into the internal (belongs to the I-TENG) and external (belongs to the O-TENG) insulated electrical parts, followed by many other trenches carved on both two parts, forming two complementary-patterned electrode networks on each part, making every single part consist of a radial array of sectors that were mutually connected at one end. As each adjacent network belongs to the opposite electrode, the two networks from each part can be regarded as two electrodes. In addition, the distance between the rotator and stator should be adjusted properly, making the arched part of FEP film completely contact only one network without covering the adjacent one.

Electrical Output Measurements: For the purpose of performance evaluation, the open-circuit voltage and short-circuit current of the TENG device were measured by a Keithley 6514 system electrometer. For the multichannel measurement and demonstration, the voltage outputs were measured by an ADC (NI 9220, 16-channel voltage measurement module, ±10 V, National Instrument).

Supporting Information

Supporting Information is available from the Wiley Online Library or from the author.

Conflict of Interest

The authors declare no conflict of interest.

Data Availability Statement

Research data are not shared.

[1] L. Atzori, A. Iera, G. Morabito, *Comput. Networks* **2010**, *54*, 2787.

[2] J. Li, C. Wu, I. Dharmasena, X. Ni, W. Ding, *Intell. Converged Networks* **2020**, *1*, 115.

[3] J. H. Nord, A. Koohang, J. Paliszkiewicz, *Expert Syst. Appl.* **2019**, *133*, 97.

[4] L. Xie, X. Chen, Z. Wen, Y. Yang, J. Shi, C. Chen, M. Peng, Y. Liu, X. Sun, *Nano-Micro Lett.* **2019**, *11*, 39.

[5] T. Li, H. Fan, J. García, J. M. Corchado, *Inf. Fusion* **2019**, *51*, 233.

[6] M. K. Stojcev, M. R. Kosanovic, L. R. Golubovic, 9th Int. Conf. on Telecommunication in Modern Satellite, Cable, and Broadcasting Services, IEEE, Piscataway, NJ **2009**, pp. 65–72.

[7] D. E. Tiliute, *Elektron. Elektrotech.* **2015**, *4*, 9.

[8] H. Shao, P. Cheng, R. Chen, L. Xie, N. Sun, Q. Shen, X. Chen, Q. Zhu, Y. Zhang, Y. Liu, Z. Wen, X. Sun, *Nano-Micro Lett.* **2018**, *10*, 198.

[9] Q. Zeng, Y. Wu, Q. Tang, W. Liu, J. Wu, Y. Zhang, G. Yin, H. Yang, S. Yuan, D. Tan, C. Hu, X. Wang, *Nano Energy* **2020**, *70*, 104524.

[10] Y. Wu, Q. Zeng, Q. Tang, W. Liu, G. Liu, Y. Zhang, J. Wu, C. Hu, X. Wang, *Nano Energy* **2020**, *67*, 104205.

[11] G. Liu, J. Chen, Q. Tang, L. Feng, H. Yang, J. Li, Y. Xi, X. Wang, C. Hu, *Adv. Energy Mater.* **2018**, *8*, 1703086.1.

[12] O. Artal, O. Pizarro, H. H. Sepúlveda, *Renewable Energy* **2019**, *139*, 496.

[13] H. J. Seok, A. Ali, J. H. Seo, H. H. Lee, H. K. Kim, *Sci. Technol. Adv. Mater.* **2019**, *20*, 389.

[14] Z. Wen, H. Guo, Y. Zi, M. Yeh, X. Wang, J. Deng, J. Wang, S. Li, C. Hu, L. Zhu, Z. L. Wang, *ACS Nano* **2016**, *10*, 6526.

[15] H. Shao, Z. Wen, P. Cheng, N. Sun, Q. Shen, C. Zhou, M. Peng, Y. Yang, X. Xie, X. Sun, *Nano Energy* **2017**, *39*, 608.

[16] C. Castro, M. Mediavilla, L. Miguel, F. Frechoso, *Energy Policy* **2011**, *39*, 6677.

[17] Y. Zhang, Q. Zeng, Y. Wu, J. Wu, S. Yuan, D. Tan, C. Hu, X. Wang, *Nano-Micro Lett.* **2020**, *12*, 232.

[18] C. Jung, D. Schindler, *Sustainable Energy Technol. Assess.* **2020**, *42*, 100852.

[19] C. Archer, M. Jacobson, *J. Geophys. Res.: Oceans* **2005**, *110*, D12.

[20] J. M. Carrasco, L. G. Franquelo, J. T. Bialasiewicz, E. Galván, R. Guisado, M. Prats, J. I. León, M. Narciso, *IEEE Trans. Ind. Electron.* **2006**, *53*, 1002.

[21] C. Zhe, J. M. Guerrero, F. Blaabjerg, *IEEE Trans. Power Electron.* **2009**, *24*, 1859.

[22] D. Xiang, L. Ran, P. J. Tavner, S. Yang, *IEEE Trans. Energy Convers.* **2006**, *21*, 652.

[23] Y. Lei, A. Mullane, G. Lightbody, R. Yacamini, *IEEE Trans. Energy Convers.* **2006**, *21*, 257.

[24] F. Fan, Z. Tian, Z. Wang, *Nano Energy* **2012**, *1*, 328.

[25] W. Wang, J. Xu, H. Zheng, F. Chen, J. Kory, Y. Wu, H. Wang, W. Zhang, R. Yang, *Nanoscale* **2018**, *10*, 14747.

[26] C. Rodrigues, C. Alves, J. Puga, A. Pereira, J. Ventura, *Nano Energy* **2016**, *30*, 379.

[27] Y. Zi, H. Guo, Z. Wen, M. Yeh, C. Hu, Z. Wang, *ACS Nano* **2016**, *10*, 4797.

[28] H. Guo, Z. Wen, Y. Zi, M. H. Yeh, J. Wang, L. Zhu, C. Hu, Z. L. Wang, *Adv. Energy Mater.* **2016**, *6*, 1501593.

[29] Y. Wu, S. Kuang, H. Li, H. Wang, R. Yang, Y. Zhai, G. Zhu, Z. L. Wang, *Adv. Mater. Technol.* **2018**, *3*, 1800166.

[30] L. B. Huang, W. Xu, G. Bai, M. C. Wong, Z. Yang, J. Hao, *Nano Energy* **2016**, *30*, 36.

[31] J. Wang, L. Pan, H. Guo, B. Zhang, R. Zhang, Z. Wu, C. Wu, L. Yang, R. Liao, Z. L. Wang, *Adv. Energy Mater.* **2019**, *9*, 1802892.

[32] J. Wang, Z. Wu, L. Pan, R. Gao, B. Zhang, L. Yang, H. Guo, R. Liao, Z. L. Wang, *ACS Nano* **2019**, *13*, 2587.

[33] L. Pan, J. Wang, P. Wang, R. Gao, Y. C. Wang, X. Zhang, J. J. Zhou, Z. L. Wang, *Nano Res.* **2018**, *11*, 4062.

[34] S. Chen, C. Gao, W. Tang, H. Zhu, Y. Han, Q. Jiang, T. Li, X. Cao, Z. Wang, *Nano Energy* **2015**, *14*, 217.

[35] Y. Xie, S. Wang, L. Lin, Q. Jing, Z. H. Lin, Z. Niu, Z. Wu, Z. L. Wang, *ACS Nano* **2013**, *7*, 7119.

[36] M. Perez, S. Boisseau, M. Geisler, G. Despesse, J. L. Reboud, *J. Phys.: Conf. Ser.* **2016**, *773*, 012118.

[37] H. Yong, J. Chung, D. Choi, D. Jung, M. Cho, S. Lee, *Sci. Rep.* **2016**, *6*, 33977.

[38] J. Wang, W. Ding, L. Pan, C. Wu, H. Yu, L. Yang, R. Liao, Z. L. Wang, *ACS Nano* **2018**, *12*, 3954.

[39] G. Zhu, J. Chen, T. Zhang, Q. Jing, Z. Wang, *Nat. Commun.* **2014**, *5*, 5.